AIP | Journal of Renewable and Sustainable Energy

Investigating wind turbine impacts on near-wake flow using profiling lidar data and large-eddy simulations with an actuator disk model

Jeffrey D. Mirocha, Daniel A. Rajewski, Nikola Marjanovic, Julie K. Lundquist, Branko Kosović, Caroline Draxl, and Matthew J. Churchfield

Citation: Journal of Renewable and Sustainable Energy **7**, 043143 (2015); doi: 10.1063/1.4928873
View online: http://dx.doi.org/10.1063/1.4928873
View Table of Contents: http://scitation.aip.org/content/aip/journal/jrse/7/4?ver=pdfcov
Published by the AIP Publishing

Investigating wind turbine impacts on near-wake flow using profiling lidar data and large-eddy simulations with an actuator disk model

Jeffrey D. Mirocha,[1,a)] Daniel A. Rajewski,[2] Nikola Marjanovic,[1,3] Julie K. Lundquist,[4,5] Branko Kosović,[6] Caroline Draxl,[5] and Matthew J. Churchfield[5]

[1]*Lawrence Livermore National Laboratory, 7000 East Avenue, Livermore, California 94551, USA*
[2]*Department of Agronomy, Iowa State University, 3132 Agronomy Hall, Ames, Iowa 50011-1010, USA*
[3]*Department of Civil and Environmental Engineering, University of California, MC1710, Berkeley, California 94770-1710, USA*
[4]*Department of Atmospheric and Oceanic Sciences, University of Colorado at Boulder, 311 UCB, Boulder, Colorado 80309-0311, USA*
[5]*National Renewable Energy Laboratory, 15013 Denver West Parkway, Golden, Colorado 80401-3305, USA*
[6]*National Center for Atmospheric Research, P. O. Box 3000, Boulder, Colorado 80307, USA*

(Received 5 November 2014; accepted 7 August 2015; published online 27 August 2015)

Wind turbine impacts on the atmospheric flow are investigated using data from the Crop Wind Energy Experiment (CWEX-11) and large-eddy simulations (LESs) utilizing a generalized actuator disk (GAD) wind turbine model. CWEX-11 employed velocity-azimuth display (VAD) data from two Doppler lidar systems to sample vertical profiles of flow parameters across the rotor depth both upstream and in the wake of an operating 1.5 MW wind turbine. Lidar and surface observations obtained during four days of July 2011 are analyzed to characterize the turbine impacts on wind speed and flow variability, and to examine the sensitivity of these changes to atmospheric stability. Significant velocity deficits (*VD*) are observed at the downstream location during both convective and stable portions of four diurnal cycles, with large, sustained deficits occurring during stable conditions. Variances of the streamwise velocity component, σ_u, likewise show large increases downstream during both stable and unstable conditions, with stable conditions supporting sustained small increases of σ_u, while convective conditions featured both larger magnitudes and increased variability, due to the large coherent structures in the background flow. Two representative case studies, one stable and one convective, are simulated using LES with a GAD model at 6 m resolution to evaluate the compatibility of the simulation framework with validation using vertically profiling lidar data in the near wake region. Virtual lidars were employed to sample the simulated flow field in a manner consistent with the VAD technique. Simulations reasonably reproduced aggregated wake *VD* characteristics, albeit with smaller magnitudes than observed, while σ_u values in the wake are more significantly underestimated. The results illuminate the limitations of using a GAD in combination with coarse model resolution in the simulation of near wake physics, and validation thereof using VAD data. [http://dx.doi.org/10.1063/1.4928873]

I. INTRODUCTION

Wind turbine wakes influence the performance of turbines located downstream primarily via velocity deficits (*VD*) and increased turbulence. These characteristics of turbine wakes

[a)]Electronic mail: jmirocha@llnl.gov

diminish the energy available for conversion to power and amplify stress loading on turbine components. While wake characteristics are widely reported within the literature (e.g., Thomsen and Sørenson (1999) and Vermeer *et al.* (2003)), present understanding of wake structure and dynamics remains incomplete. Although early studies of wind turbine wakes noted their variability in response to changes of atmospheric stability (Högström *et al.,* 1988 and Magnusson and Smedman, 1994), current understanding of the details of such variability is constrained both by a shortage of observations of key wake parameters (e.g., turbulence, wake spreading and meander, and wake interactions), and by limitations of present day tools used for computational investigations (e.g., Sanderse *et al.* (2011); Troldborg *et al.* (2011); and Mirocha *et al.* (2014)). Many of the more sophisticated computational approaches undertaken recently, such as those using large-eddy simulations (LESs) with actuator turbine models, have focused primarily on power degradation of downstream turbines (e.g., review by Mehta *et al.* (2014)).

Much understanding of wake characteristics has been gleaned from analysis of turbine power data in large wind farms. For example, Hansen *et al.* (2012) used power production data to confirm previous studies (Magnusson and Smedman, 1994) that relied on meteorological measurements to suggest that wake velocity deficits are larger in stable conditions. However, analysis of power data provides limited insights into wake dynamics. Observations of wakes using higher-frequency instrumentation on downstream towers have provided additional insights into wake properties (e.g., Magnusson and Smedman (1994); Elliott and Barnard (1990); and Rajewski *et al.* (2014)).

Remote sensing technologies such as sodars, lidars, and radars can provide measurements of some important of atmospheric parameters in the vicinity of operating turbines (e.g., Högström *et al.* (1988); Barthelmie *et al.* (2003); Nygaard (2011); Hirth *et al.* (2012); Rhodes and Lundquist (2013); Smalikho *et al.* (2013); and Iungo and Porté-Agel (2013)). While these technologies are highly transportable, permitting the sampling of flow at multiple locations, they typically sample either over large volumes or at low temporal frequencies, which can hinder the interpretation of turbulence phenomena (Sathe *et al.,* 2011), or sample in unique, platform-dependent manners, which must be accounted for to enable proper interpretation. Moreover, such systems are sensitive to cloud, precipitation, and turbidity, which impacts both data recovery rates and measurement accuracy (Aitken *et al.,* 2012). Despite these limitations, remote sensing platforms are increasingly being utilized in various wind energy applications due to their flexibility and rapidly evolving capabilities.

Further, the broad application of scanning remote sensing technologies has greatly increased the data available to characterize wake properties and processes. The Turbine Wake Inflow Characterization Study (TWICS, Smalikho *et al.,* 2013 and Aitken *et al.,* 2014a) utilized a high-resolution scanning lidar to evaluate both inflow and wakes within 20 rotor diameters D of a 2.3 MW turbine. Observations document several wake characteristics, including downstream evolution, spreading, meandering, and the role of atmospheric stability. Aitken and Lundquist (2014) used observations from a nacelle-mounted scanning lidar to characterize the turbine's wake as it evolves downwind, finding that both the wake expansion rate and the amplitude of wake meandering are greater during high ambient turbulence intensity and daytime conditions, as compared to low turbulence and nocturnal conditions. Dual-Doppler radar (Hirth *et al.,* 2012) has enabled documentation of turbine wakes extending to 30D downwind.

Scanning lidar data have recently been utilized to evaluate and improve computational flow solvers, which can be used to provide additional insight into wake dynamics. Mirocha *et al.* (2014) utilized a generalized actuator disk (GAD) turbine wake model implemented into the Weather Research and Forecasting (WRF; Skamarock *et al.,* 2008) model to perform LES of portions of the TWICS experiment. The WRF model was chosen due to its ability to represent atmospheric physical processes impacting turbine performance not typically included in computational frameworks used to investigate turbine-atmosphere interactions (e.g., Sanderse *et al.* (2011)). Their WRF-LES-GAD simulations showed generally good agreement with observed characteristics of both the inflow and the wakes observed in the TWICS study, and revealed a strong relationship between wake attenuation and convective instability. Aitken *et al.* (2014b) utilized a similar computational framework to investigate wake effects during stable conditions

in a different experiment with a nacelle-mounted scanning lidar, and also obtained generally good agreement with the observations.

Two commercially available vertically pointing pulsed Doppler lidar systems were recently deployed during the Crop Wind Energy Experiment (CWEX-11; Rajewski *et al.*, 2013 and Rhodes and Lundquist, 2013) to sample the flow both upstream and downstream of an operating 1.5 MW turbine. Comparison of profiles derived from velocity-azimuth display (VAD) data, at upstream and downstream locations, indicates both large VD values, and significant enhancements of turbulence downstream. The resulting dataset provides an opportunity to evaluate the use of such commercially available lidar systems in combination with emerging computational techniques, to better understand and simulate relevant atmospheric physics influencing flows within wind farms.

Recently Churchfield *et al.* (submitted) utilized CWEX-11 data to validate simulations using both WRF and the Open-source Field Operations And Manipulations (OpenFOAM; http://www.openfoam.com) CFD toolbox, for both mesoscale and microscale simulations, respectively, in anticipation of future validation studies using a coupled mesoscale-microscale simulation tool, within which wind turbines will be simulated using actuator line models (e.g., Churchfield *et al.* (2012)).

The present study complements Churchfield *et al.* (submitted) by utilizing CWEX-11 data to evaluate the representation of turbine wake characteristics using the WRF-LES-GAD simulation framework. Whereas previous validation studies of the WRF-LES-GAD framework utilized scanning lidar data, with corresponding sampling strategies for model validation, herein we utilize data and model sampling strategies consistent with the two vertically profiling lidar systems deployed during CWEX-11, placed both upstream and downstream from an operating turbine, to sample both the undisturbed inflow and flow within the near-wake region of a 1.5 MW wind turbine. Section II describes the field campaign and instrumentation, analyzes data during periods featuring inflow in alignment with the lidars and the turbine, and identifies two case studies for simulation. Section III describes the computational setup, Sec. IV describes the results, and Sec. V provides a discussion and conclusions.

II. OBSERVATIONS

Data from two 48-h periods of CWEX-11 are selected for investigation. These periods feature predominantly southerly wind direction and generally fair weather, enabling characterization of turbine effects under conditions maximizing lidar operation and alignment of the lidars and the turbine with the flow. Two WindCUBE profiling lidars (Version 1) from the University of Colorado and the National Renewable Energy Laboratory (CU/NREL) were situated within a 300 MW wind farm in Central Iowa, as described in Rajewski *et al.* (2013). Figure 1 shows the position of the two lidars, approximately $2.11D$ to the south ($L1$) and $3.22D$ to the north ($L2$) of a turbine T, as well as the trajectories of the beams along which the VAD (the lidar manufacturer describes the sampling strategy as Doppler Beam Swinging (DBS), which is a subset of the VAD technique) data were obtained. Here, $D = 77$ m is the rotor diameter of the GE 1.5SLE wind turbine, with a hub height of 80 m. Additional attributes of Fig. 1 reflect details of the computational setup and are described in Sec. III.

Lidar performance at CWEX-11 was described in Rhodes and Lundquist (2013), who include a detailed discussion of one of the case studies explored herein and a more detailed map of the lidar and other sensor locations relative to the turbine. Profiles of wind speed (U), wind direction (λ), and variance of the streamwise velocity component (σ_u), averaged over 2-min intervals, are utilized herein to examine the impacts of the turbine on the flow, and to force and evaluate simulations. Herein, streamwise denotes the southerly flow component intersecting both lidars and the turbine. The lidar data were averaged in time to provide 2-min averages of scalar wind speed U and λ, as well as σ_u at ten measurement heights spanning 40–220 m above ground level (z), at 20 m intervals. A velocity deficit $VD = 100 \times (U_{L1} - U_{L2})/U_{L1}$, where subscripts $L1$ and $L2$ refer to the lidar locations (shown in Fig. 1), can be calculated to assess the magnitudes of the wind speed changes in the wake

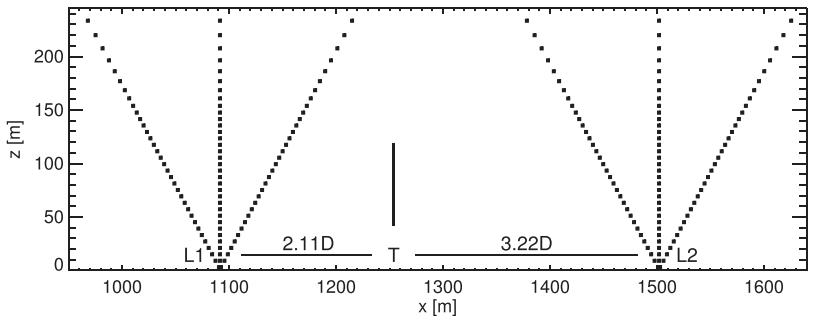

FIG. 1. Layout of turbine (T) and upstream ($L1$) and downstream ($L2$) lidars at CWEX-11, along the streamwise (x) direction. Filled squares show model heights along the beam paths from the simulations. The fourth beam from each lidar is behind the vertical beams in this projection. The x-axis shows distance from the inflow plane of the simulation domain.

relative to upstream values. $\Delta\sigma_u = \sigma_{u,L1} - \sigma_{u,L2}$ can be used to quantify the wake impact on variability of the streamwise flow component, u; a proxy for enhancement of turbulence.

Additional instrumentation at CWEX-11 provides other surface and flow parameters within the lowest 10 m of the atmosphere, as described in Rajewski *et al.* (2013). Several of these additional parameters, including temperatures at 10 (T_{10}), and 2 (T_2) m above the surface, and friction velocity (u_*), the Obukhov length (L), and surface sensible heat flux (H_S), obtained from instruments at 4.5 m above the surface, are utilized herein to better characterize the meteorological conditions and to provide forcing for the simulations. Here, $u_* = [(\tau^s_{13})^2 + (\tau^s_{23})^2]^{1/4}$, with τ^s_{i3}, $i = 1, 2$, the vertical fluxes of momentum in the streamwise and spanwise directions, respectively, at the surface, and $L = [-u_*^3\theta_{v0}]/[\kappa g H_S]$, with $\kappa = 0.4$ the von Kármán constant, g the gravitational acceleration, and $\theta_{v0} = 290$ K a reference value of the virtual potential temperature $\theta_v = \theta(1 + 0.61q_v)$, with q_v the water vapor mixing ratio, and $\theta = T(p_0/p)^{R/c_p}$ the potential temperature, with p the pressure, $p_0 = 1 \times 10^5$ Pa a reference value, $R = 287$ J kg^{-1} K^{-1} the dry air gas constant, and $c_p = 1004$ J kg^{-1} K^{-1} the specific heat of dry air at constant pressure. Values of u_*, L, and H_S utilized herein are 10-min averages.

The 48-h period of 9 July 00:00:00 through 10 July 23:58:00 UTC is described in Figure 2. Large VD values (Fig. 2(a)) are observed when λ (Fig. 2(d)) is aligned with the lidars and the turbine, with positive VD indicating flow speed reductions in the wake. The large VD values generally coincide with enhancements of σ_u (Fig. 2(b)). The time series of U (Fig. 2(c)) and λ (Fig. 2(d)) from the upstream lidar location $L1$, at five altitudes within the rotor swept area, suggest variable stratification, with stable conditions during the overnight hours, indicated by large differences of U and λ with height. Atmospheric stability is directly assessed with H_S and zL^{-1} (Fig. 2(e)), with $z = 4.5$ m the sensor height. Missing data indicate either nonoperation of one or both lidars (entire profile missing), or either precipitation or insufficient backscatter (missing upper portion only). As lidar measurement volume expands with altitude, the distances between the lidar beams are likely wider than the wake at altitudes of 120 m and above (Rhodes and Lundquist, 2013). As such, data from above 120 m may not be used to explore vertical wake propagation.

The data as presented in Fig. 2 reveal relationships between the lidar-observed VD and $\Delta\sigma_u$ and inflow characteristics. Large VD and $\Delta\sigma_u$ values are seen to occur episodically throughout the entire period. During the daytime hours, large values of these parameters can occur irrespective of inflow direction, due to large magnitudes of background variability in the convectively forced flow. During the overnight hours, when conditions are stable ($zL^{-1} > 0$), background σ_u values are lower, and large VD and $\Delta\sigma_u$ values are only observed when λ is close to 180°, and exhibit less variability in time.

Figure 3 shows the same parameters from the second 48 h period, 16 July 00:00:00 through 17 July 23:58:00 UTC, part of which is discussed in Rhodes and Lundquist (2013). Trends similar to those from the previous period are again observed, such as the sensitivity of VD and $\Delta\sigma_u$ to inflow direction and changes of the sign and magnitude of H_S and zL^{-1}. During both periods, VD and $\Delta\sigma_u$ values appear to be only minimally affected by changes of U.

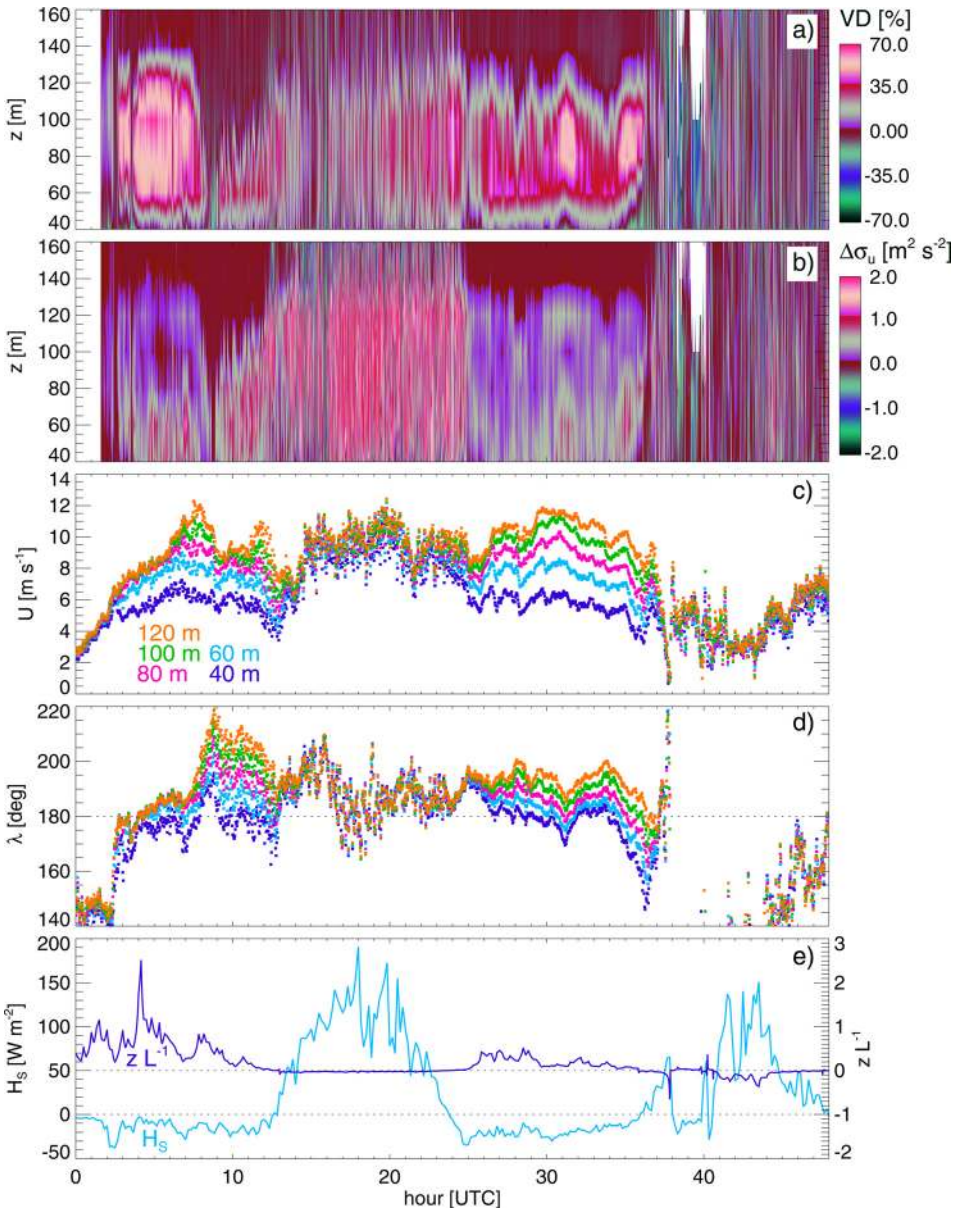

FIG. 2. Atmospheric and surface parameters during 9 July 00:00:00 through 10 July 23:58:00 UTC, including time-height sections of (a) velocity deficit, VD, and (b) differences of the variance of the streamwise velocity component, $\Delta\sigma_u$, between the upstream and downstream lidars, and time-series of (c) wind speed, U, and (d) direction, λ, from the upstream lidar, at heights of 40, 60, 80, 100, and 120 m, and (e) surface sensible heat flux, H_S, and Monin-Obukhov stability parameter $z\,L^{-1}$.

The relationships between VD, $\Delta\sigma_u$, and atmospheric stability are further examined in Figs. 4 and 5. Figure 4 shows VD as a function of λ, with color indicating the concurrent H_S value. The intervals were chosen to delineate moderately stable, weakly stable, near neutral to weakly convective, and moderately convective conditions, with roughly equal numbers of data points within each interval, as described in the legend. Consistent with Figs. 2 and 3, the largest positive VD values (Fig. 4) are again observed during stable periods for which $H_S < 0$. During convective periods, when $H_S > 0$, VD tends to be positive and smaller in magnitude on average, with considerably higher variability. The range of large VD values for $H_S > 0$ is consistent with more rapid wake spreading during convective conditions. This large range, however, could also reflect the limitations of lidar sampling of wakes during conditions with large background variability. The displacement of the largest VD values toward increasing λ with increasing

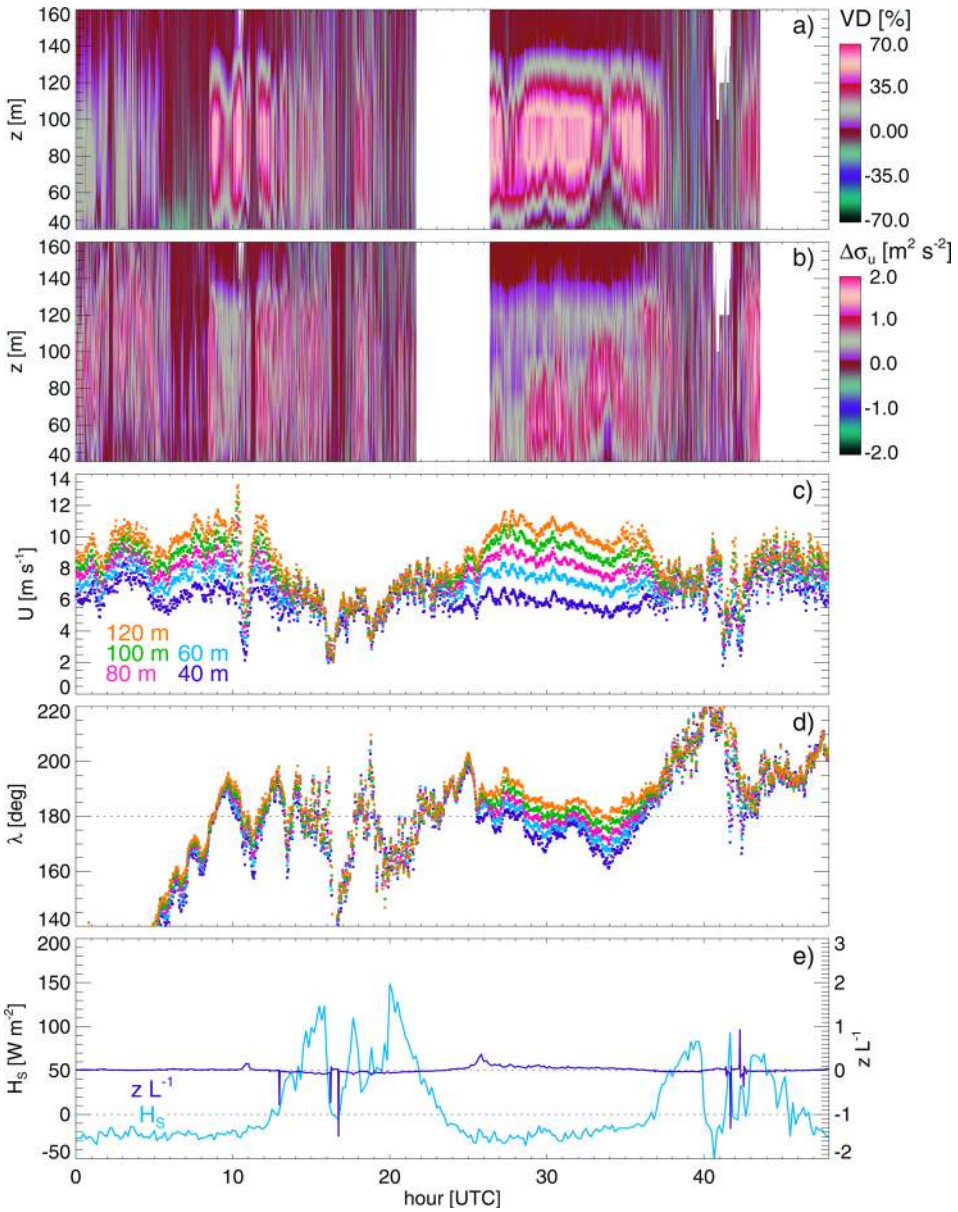

FIG. 3. Atmospheric and surface parameters during 16 July 00:00:00 through 17 July 23:58:00 UTC, as in Fig. 2.

height is consistent with the rotation of the wind vector with height, for which large increases were frequently observed overnight (see Figs. 2(d) and 3(d)), similar to the tower measurements of Walton *et al.* (2014) and lidar measurements of Vanderwende *et al.* (2015). During stable conditions, *VD* values at the higher altitudes attenuate in peak magnitude, and fall to nearly zero at values of $\lambda \cong 180 \pm 15^{\circ}$. The reduced peak magnitudes are likely due to the lidar sampling strategy missing larger portions of the wakes at higher heights (Rhodes and Lundquist, 2013), while the attenuation to nearly zero for larger values of λ from 180° indicates that wakes are not sampled at all by the downwind lidar. The slight increases of *VD* for large departures of λ from 180° are consistent with the presence of other turbines within the row approximately 5D to each side in the spanwise direction.

Acknowledging the limitations of VAD data to accurately sample the cross-stream flow component within the wake (as detailed in Lundquist *et al.* (2015)), we note that the asymmetries of *VD* about their maxima are consistent with counterclockwise wake rotation (opposite

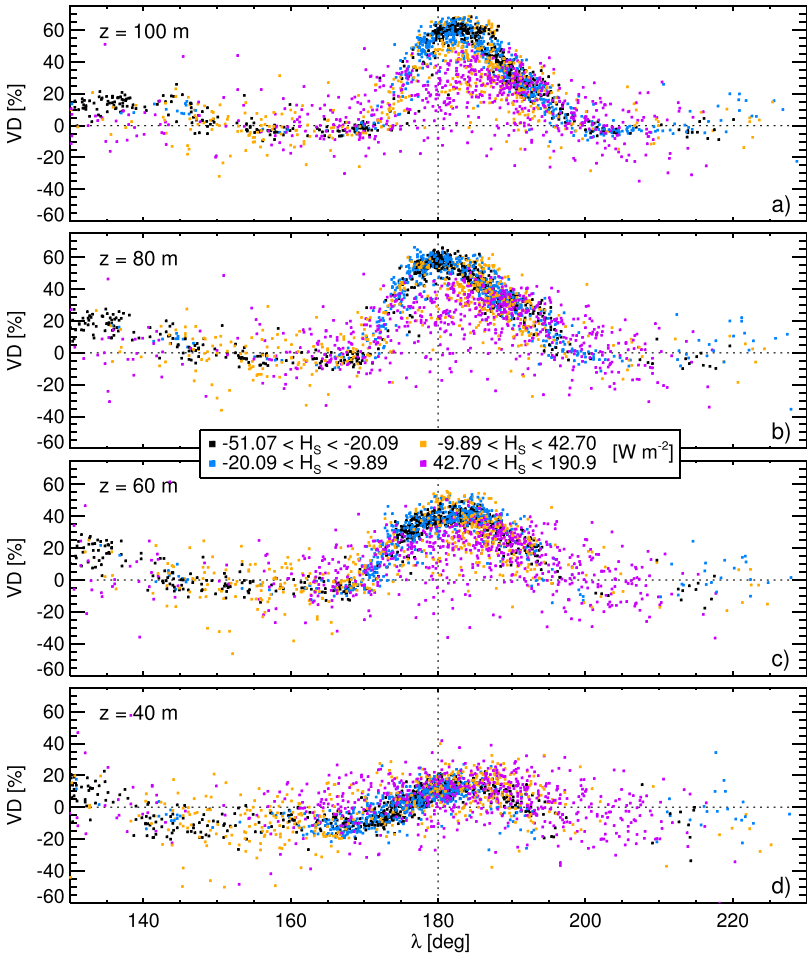

FIG. 4. *VD* as a function of λ, at the four heights nearest the turbine rotor swept area, with color indicating the concurrent value of H_S.

the clockwise rotation of the turbine), as such rotation would be expected to transport higher momentum air from aloft downward on the decreasing λ side of the turbine, while advecting lower momentum air upward, augmenting *VD* values on the increasing λ side. The small positive *VD* values for $140^\circ < \lambda < 160^\circ$ at the lowest heights are likewise consistent with an acceleration of the flow between the turbines within the row, and beneath the turbine rotor.

In addition to velocity deficits, operating turbines also impart turbulence to the flow. Figure 5 presents $\Delta\sigma_u$ values, as in Fig. 4, as a proxy for turbulence. Unlike *VD*, $\Delta\sigma_u$ shows much larger values during convective conditions; however, also intermittently shows significant decreases at the downstream lidar, due to the large spatiotemporal variability of σ_u in the ambient convectively forced flow. While the magnitudes of $\Delta\sigma_u$ are smaller during stable conditions, they are consistently positive, indicating more clearly that the turbine is increasing σ_u on average. The asymmetries of $\Delta\sigma_u$ with respect to the corresponding *VD* maxima in Fig. 4, with slightly larger $\Delta\sigma_u$ values on the decreasing λ side of the turbine, are again consistent with wake rotation. The counterclockwise aggregate wake rotation would be expected to transport downward on that side of the turbine larger values of σ_u being produced near the top of the rotor, where mean wind speed is greater.

A better understanding of *VD* and $\Delta\sigma_u$ in relation to inflow direction and atmospheric stability can provide insights to improve wind plant design and operation. Simulation tools capable of capturing these relationships could assist in optimization of new plant design and operations of existing arrays. Next, we investigate the representation of *VD* and $\Delta\sigma_u$ in relation to inflow

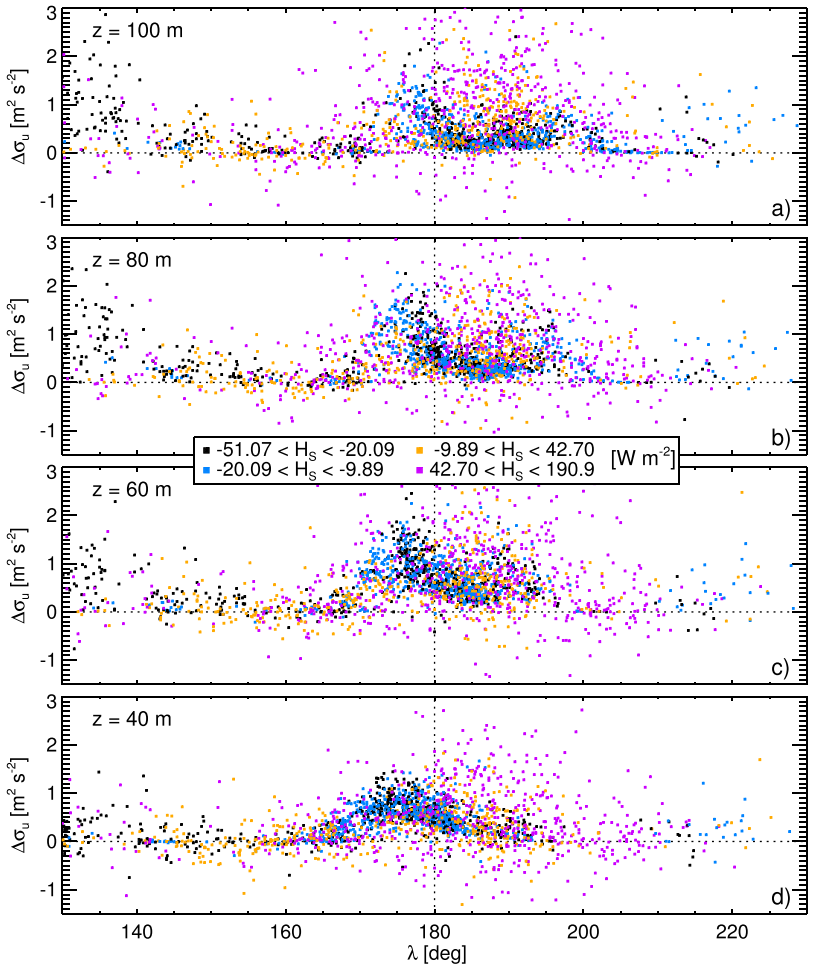

FIG. 5. $\Delta\sigma_u$, as in Fig. 4.

direction and atmospheric stability in an atmospheric LES code with an actuator disk wind turbine model.

III. SIMULATION SETUP

A. Computational framework

The computational framework employed herein is the WRF model, with a GAD wind turbine parameterization, as described in Mirocha *et al.* (2014) and Aitken *et al.* (2014b). As not all of the parameters required for the GAD were available for the GE 1.5 MW SLE turbine operating during CWEX-11, we instead use the Generic Penn State University 1.5 MW turbine, with the same diameter (77 m) and hub height (80 m), and a similar power curve (Schmitz, 2012). Following those studies, a fine LES with horizontal grid spacing $\Delta x = 6$ m is nested within a coarser LES, using $\Delta x = 18$ m. The vertical grid spacing is approximately $\Delta z = 6$ m on both domains, with constant Δz between the surface and 200 m, above which Δz increases by 5% per vertical grid cell, up to a model top of 3077 m. The outer domain uses periodic lateral boundary conditions, which permits development of quasi-equilibrium turbulent boundary layer inflow and outflow for the finer LES nested within. The GAD operates within the nested domain. Physical and computational dimensions of the simulations are provided in Table I.

As WRF uses a pressure-based vertical coordinate $\eta(z) = (p(z) - p_t)/(p_S - p_t)$, where p_t and p_S are the pressure values at the model top and surface, specified Δz values were converted to η using the hypsometric equation (e.g., Holton (1980)), with $p_S = 1 \times 10^5$ Pa, and

TABLE I. Physical and computational dimensions of the numerical simulations. Here n_x, n_y, and n_z are the number of grid points in the x, y, and z directions; Δh and Δz are the horizontal and vertical grid spacings; and L_x, L_y, and L_z represent the domain dimensions. Δz values are stretched above 200 m, as described in the text. The nested domain's lower left corner begins at $[i, j] = [106, 11]$ in the outer domain, where i and j indicate grid cell indices in the x and y directions, respectively.

	n_x	n_y	n_z	Δx (m)	Δz (m)	L_x (m)	L_y (m)	L_z (m)
Outer domain	242	57	67	18	6	4338	1008	3077
Nested domain	376	106		6		2250	630	

temperatures from the standard atmosphere. The upper boundary conditions are $w = 0$, and free-slip for u and v, with Rayleigh damping applied within 1 km of the model top, with a magnitude of 0.003 s^{-1}.

The surface boundary condition enforces $w = 0$ and utilizes Monin-Obukhov similarity theory to prescribe fluxes of momentum, u_* and heat, H_S. The subgrid fluxes of momentum above the surface are obtained from the nonlinear backscatter and anisotropy (NBA) model, while those for heat were prescribed using the Smagorinsky closure. Details of these formulations are provided in Appendix A.

As the terrain and land cover at CWEX are nearly uniform on the spatial scales impacting the computational framework, the surface of the computational domains is flat, and two roughness length values of $z_0 = 0.15$ and 0.2 m, representative of corn with an average height of around 1–3 m, were used. Given the absence of precipitation, moisture is neglected, and the effects of solar radiation are incorporated via H_S and a surface temperature tendency ΔT_S, simplifying the simulations.

B. Case studies

Data from the four days described in Sec. II were queried for case studies to examine the efficacy of the computational framework. Criteria included inflow in close alignment with the turbine and instrumentation ($\lambda \cong 180^\circ$), consistent wind speeds within the envelope of turbine operation, flow, and surface conditions sufficiently uniform to be reasonably approximated using idealized forcing, and data available from both lidars. The periods best satisfying these criteria are the afternoon of 9 July and the early morning of 17 July.

1. Stable case study

Figure 6 shows profiles of U, λ, and σ_u from approximately midnight through the early morning of 17 July, from $L1$. The lidar data were averaged over 10-min intervals to reduce the number of profiles plotted, simplifying visualization and identification of trends. Figure 6 shows nearly uniform vertical distributions of U with little variability in time. Profiles of σ_u show an

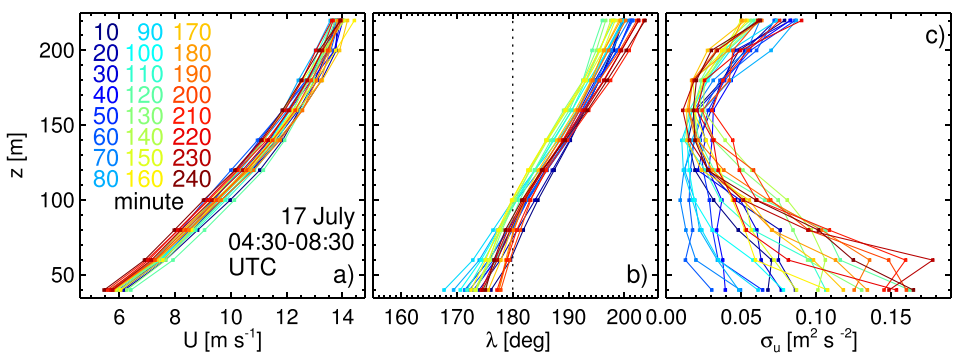

FIG. 6. 10-min average observed U (left), λ (middle), σ_u (right) profiles from $L1$ during the morning of 17 July.

upside-down boundary layer structure initially (e.g., Mahrt and Vickers (2002)), followed by gradually increasing σ_u values thereafter near the surface, with small decreases at the highest altitudes sampled. The increases of σ_u appear to coincide with slightly lower U values, yet have little discernable influence on the gradients. A more pronounced change is observed for λ, which shows a slight westward rotation of the entire profile, as well as a noticeable reduction of gradients near the surface. The mechanism for the increasing values of σ_u and corresponding changes of λ are unknown. Mechanical production is likely decreasing during the period due to decreasing values of U and shear between the lowest lidar range gate and the surface (Fig. 3(c)), however the changes of λ (Fig. 3(d)) suggest the possibility of mesoscale variability or an inertial oscillation playing a role. Additionally, surface cover comprised of nearly uniform rows of 1–3 m tall corn (Rajewski *et al.*, 2013) could have yielded a high degree of directional dependence to the streamwise flow variability near the surface.

While Fig. 2(a) suggests an additional candidate stable case study occurring during the morning of 9 July, detailed analysis of that period revealed much more significant trends of U, λ and σ_u, suggesting stronger mesoscale influences, hence was deemed less suitable for the idealized simulations comprising the focus of this study.

2. Convective case study

Figure 7 shows observed profiles of U, λ, and σ_u during the convective afternoon period of 9 July, as in Fig. 6. Other afternoon periods were not investigated due to generally poor alignment between the lidars, turbine, and the flow (see Figs. 2(d) and 3(d)). Profile shapes are generally similar throughout the afternoon of 9 July, and while some variability is observed, no indications of storm outflow or other significant mesoscale or meteorological events stand out. The magnitudes of σ_u follow closely the evolution of H_S (see Fig. 2(e)), with larger (smaller) values occurring toward the beginning (end) of the period, suggesting that the forcing can be reasonably well approximated using an idealized computational setup.

3. Case study simulation setup

Case studies from the morning of 17 July and the afternoon of 9 July were constructed for simulation. The simulations were forced using specified values of the geostrophic wind, V_g, constant in time and height. As V_g was not measured, values were fine-tuned to provide satisfactory agreement with observed U and λ over the range of lidar sampled heights. The initial θ profile was prescribed as a superposition of a mean value of 300 K and small perturbations, $\delta \in [\pm 0.25]$ K, from a pseudo-random uniform distribution, decreasing as a cubic function of height above the surface up to $z = 500$ m. Above this height, θ increases by 10 K km^{-1}, creating a capping inversion to prevent turbulence from reaching the model top. While the specified values of θ (not shown) do not match the observations, it is the vertical gradients that control buoyancy and surface exchange, the relevant physical processes. The perturbations, imposed

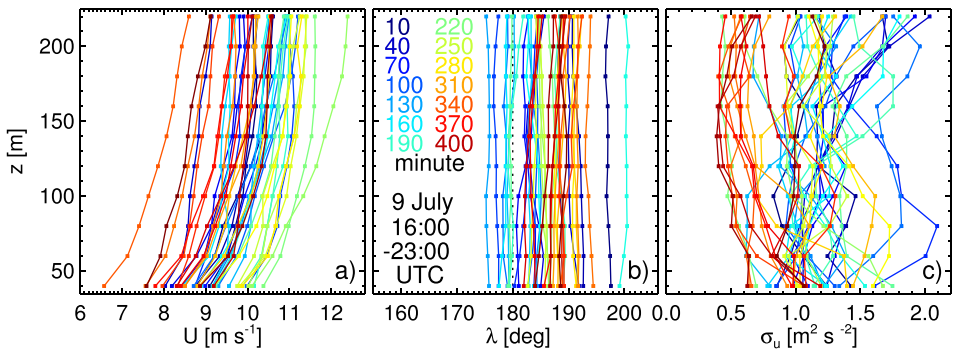

FIG. 7. 10-min average observed U (left), λ (middle), σ_u (right) profiles during the afternoon of 9 July, as in Fig. 6.

only at the beginning of the simulation, trigger the development of turbulence, which amplifies and equilibrates to the specified forcing during subsequent simulation on the outer domain.

For all simulations, the outer domain was integrated for 15 h of physical time with neutrality imposed at the surface ($H_S = 0$), allowing the solution to equilibrate to the specified geostrophic forcing chosen for each case study. At the beginning of hour 15, the stable cases were thereafter forced in two different ways, either with uniform heat fluxes (time averages of observed values), or (following Basu *et al.* (2008)) with specified values of the surface cooling rate, ΔT_S, the latter estimated from the observed near-surface temperature time series. Simulations forced with H_S utilized a linear increase from zero to the specified value during hour 15, after which the value was held constant. For simulations forced with ΔT_S, the surface temperature was uniformly prescribed as the horizontal average temperature at the first model grid point above the surface, providing neutrality in the aggregate, at the beginning of hour 15, after which subsequent cooling of T_S stabilized the flow. The convective case was forced using H_S, as in the stable case, but with a positive value of 100 W m^{-2}. The finer-scale nested domains containing the GAD were initiated from the outer domain solutions once those flow fields exhibited U and λ profiles consistent with the observations during each case study.

IV. SIMULATION RESULTS

For comparison with observations, the simulated flow field was sampled in a manner consistent with the lidars. Simulated parameter values were obtained along four beam angles, as shown in Fig. 1, which provides an illustration of the simulation sampling setup, with sampling locations $L1$ and $L2$ located 2.11 D upwind and 3.22 D downwind of the GAD, located at the turbine location T, duplicating the layout at CWEX-11. T is located at $(x, y) = (1254, 318)$ m within the nested domain, providing over 200 model grid points in the streamwise direction upon which turbulence entering the nested domain can equilibrate to the finer mesh. The filled squares show the heights of the model levels for which the horizontal velocity components were computed. The streamwise and spanwise velocity values at each beam location were obtained from bilinear interpolation using the four grid points bounding each beam in the horizontal direction. The radial components of the velocity along each beam were obtained via projection of the interpolated streamwise and spanwise velocity components onto the beams oriented in those directions. The radial velocities at each range gate were then obtained as weighted averages along each beam, using an appropriate lidar weighting function, from which the "lidar observed" streamwise and spanwise velocity components were obtained. The above operation was performed each second, after which the mean values and variances were computed over each 2-min period, for comparison with the observations. Details of the lidar weighting function and velocity retrievals are provided in Appendix B.

A. Stable case

Boundary layer structure, especially the vertical profiles of U and λ, is sensitive to small changes of the forcing during stable conditions (e.g., Basu *et al.* (2008)). Figure 8 explores this sensitivity by examining hourly averaged U and λ profiles at each hour beginning at hour 16 (1 h after the neutral spinup), forced with different values of surface parameters, ΔT_S, H_S, and z_0. All stable simulations were forced with $V_g = 11.0$ m s^{-1} and $\lambda_g = 31^\circ$ clockwise from the line between the GAD and $L2$. These values produced good agreement with observed wind speed and direction profiles at the end of the neutral spinup portions of the simulations. The two left and two right columns of Fig. 8 show sensitivity to the magnitudes of ΔT_S and H_S, respectively, while the eight bottom and eight top panels use different values of z_0, as indicated on the figure. The values of $\Delta T_S = -2/3$ K h^{-1} and $H_S = -23.5$ W m^{-2} correspond to approximate observed values of those parameters between 04:30 and 08:30 UTC. Increases of ΔT_S and H_S by 50% to -1 K h^{-1} and -34.75 W m^{-2}, respectively, as well as z_0 values increased from 0.15 and 0.20 m, are shown. Gray horizontal lines depict the range of the observed 2-m average profiles (from Fig. 6).

Simulations forced with different ΔT_S values (Figs. 8(a)–8(d) and 8(i)–8(l)) exhibit qualitatively similar behavior, with U increasing to a maximum, thereafter decreasing, while λ

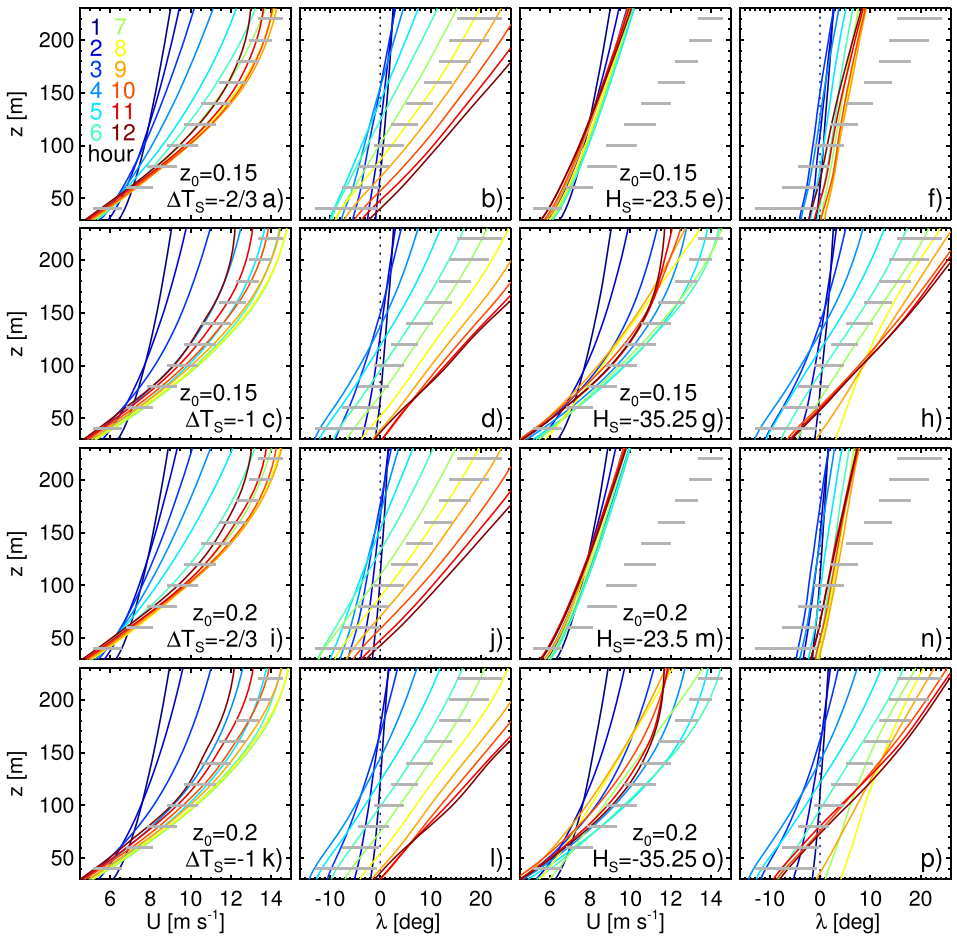

FIG. 8. Sensitivity of U and λ profiles to changes of ΔT_S, H_S and z_0, during 12 h of simulation beyond the neutrally forced quasi-equilibrium profiles. Gray horizontal lines depict the range of the observed 10-min average profiles during the 4-h case study.

continues to increase, and with the larger cooling rate producing more rapid changes of both U and λ. Simulations forced with the two H_S values (Figs. 8(e)–8(h) and 8(m)–8(p)) exhibit qualitatively different behaviors, with the smaller value yielding only small departures from the neutral quasi-equilibrium values, while larger H_S values produce rapid stabilization, similar to that resulting from the larger ΔT_S value. Simulations using values of both ΔT_S and H_S reduced by 50% to $-1/3$ K h^{-1} and $H_S = -14.75$ W m^{-2} produced only minor departures from the neutral quasi-equilibrium profiles (not shown). The impacts of changes of z_0 (upper 8 versus lower 8 panels), while nontrivial, are small compared with those of ΔT_S and H_S, over the ranges of values of those parameters investigated herein.

None of the simulated U and λ profiles remained within the bounds of the observations throughout the entire 4-h duration of the case study, suggesting potential limitations of the idealized setup. Nevertheless, good agreement of the simulated and observed profiles during subsets of the simulations provides representative flows for examination of simulated U, λ, and σ_u in response to interactions with the GAD.

Stable simulations with the GAD were executed during subsets of the simulations forced with $\Delta T_S = -2/3$ K h^{-1} and $z_0 = 0.2$ m, during times when simulated U and λ profiles most closely approximated observed values. The nested domain was initialized just prior to the profiles approaching measured values, after 5.5 h of additional simulation (21.5 h total). Results were analyzed following an additional half hour of simulation, allowing the inner domain containing the GAD, to spin up.

Figure 9 shows instantaneous horizontal cross sections of U at three heights above the surface, from the middle of the stable simulation. The dotted vertical line shows the location of the GAD, while the black squares show the volumes of the four beams of $L2$. The wake is clearly visible as reduced wind speeds downstream from the GAD, against background turbulent fluctuations. The wake intersects the $L2$ beams intermittently, with usually one or more of the beams at the edge or outside of the region of significantly lower wind speeds. These results agree with those of Aitken *et al.* (2014b) for which a similar computational framework (WRF-LES-GAD) also was found to underestimate the width of the wake in the near-wake region when compared with scanning lidar estimates.

Figure 10 shows 2-min average U (left), λ (middle), and σ_u (right) profiles from $L1$ and $L2$, during 120 min of the stable simulation. Horizontal blue and red lines show the observed range of 2-min average values from $L1$ and $L2$ over the 4-h period, with the vertical hatches indicating the mean values within each range, while light blue and orange depict simulated data from those locations, respectively. Each row shows 20 2-min average profiles obtained as λ at 80 m above the surface evolved from $\lambda < 180^\circ$ (top), to $\lambda \cong 180^\circ$ (middle), to $\lambda > 180^\circ$ (bottom), permitting discernment of directional dependence on simulated quantities.

Figure 10 shows that while the shapes and magnitudes of the simulated U, λ, and σ_u profiles are consistent with measurements at $L1$, variability is underrepresented in the simulations. Agreement at $L2$ is not as good, with the simulations failing to capture some features of the observed profiles of each quantity. Reductions of U are underrepresented between 80 and 120 m, with the smallest discrepancies occurring when $\lambda < 180^\circ$. While simulated U values above the rotor swept area are slightly greater than the observed values, those within the rotor swept area remain within the observed range.

Simulated λ profiles at $L2$ show significant departures from the observations within the upper portion of the rotor swept area, with the observations showing pronounced increases that the simulations fail to capture. Given the inherent difficulties of obtaining spanwise velocities in turbine wakes using profiles obtained from VAD lidar data, discussed in Lundquist *et al.* (2015), the observed λ values at $L2$ should be interpreted with caution. However, we note that the simulated flow field, sampled in a manner consistent with the lidar, does not capture that observed feature.

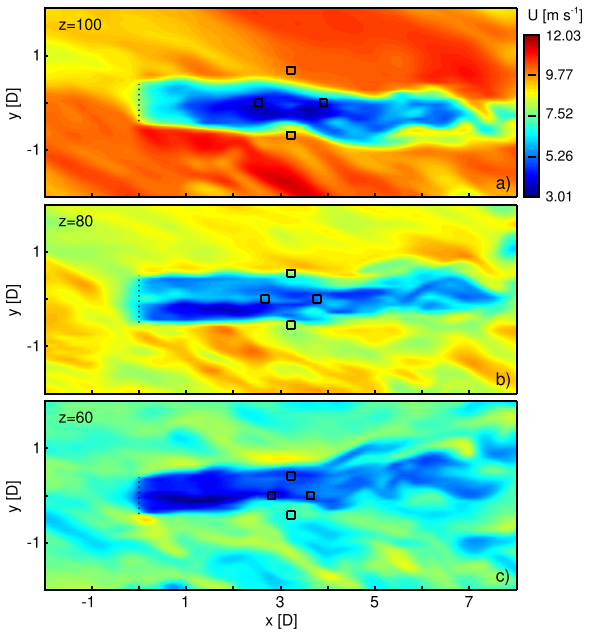

FIG. 9. Representative instantaneous horizontal cross sections of U at three heights above the surface, from the stable simulation. The dotted vertical line shows the location of the GAD, while black squares show the four beams of $L2$.

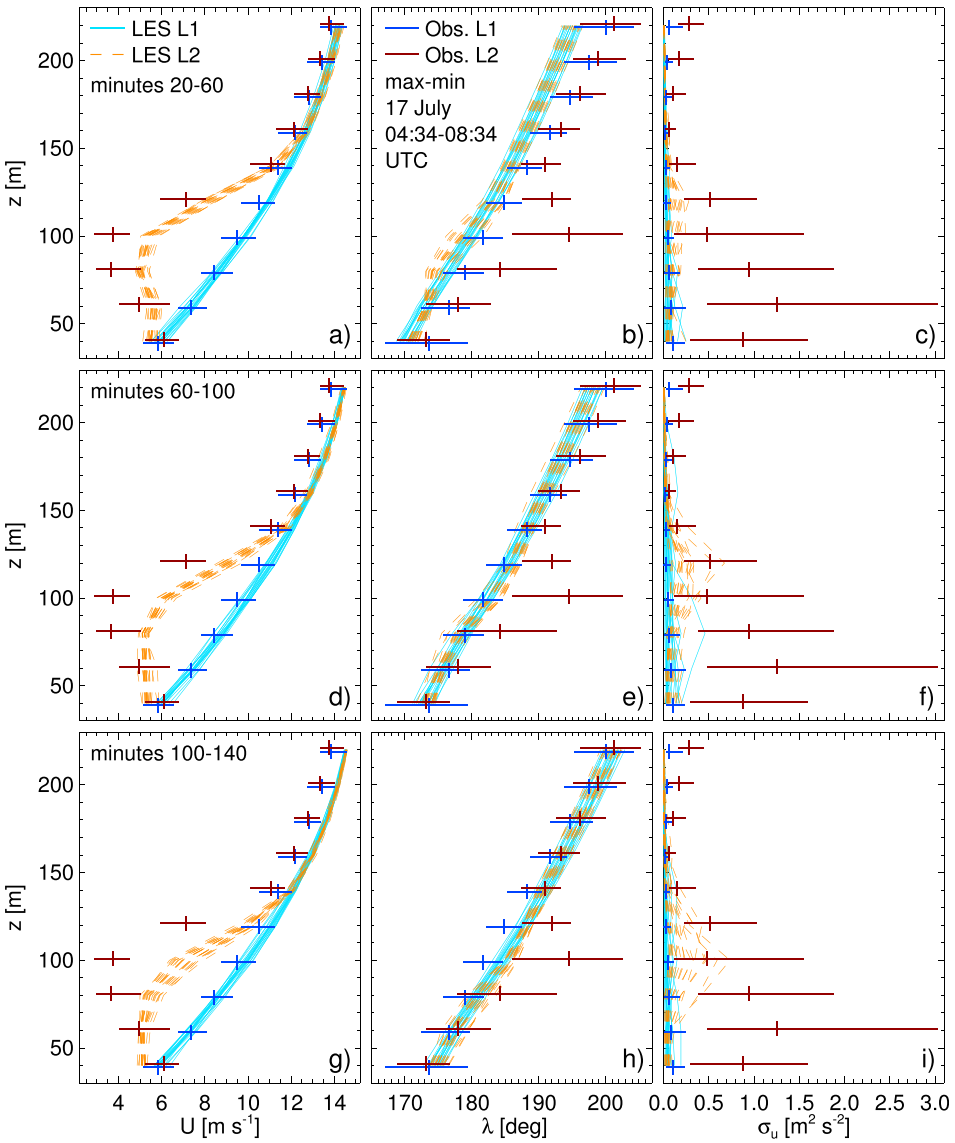

FIG. 10. 2-min average profiles of U (left), λ (middle) and σ_u (right) over 1.5 h of the stable simulation, for $\lambda < 180°$ (top), $\lambda \cong 180°$ (middle), and $\lambda > 180°$ (bottom). Light blue and orange profiles are from locations $L1$ and $L2$, while horizontal blue and red lines show the observed range of 2-min average values from $L1$ and $L2$, respectively, with the vertical hatch indicating the mean value within each range.

Simulated σ_u values likewise show departures from the observations at both $L1$ and $L2$. The simulated σ_u profiles at $L1$ exhibit similar magnitudes to the observations at around 100 m, however fail to capture the increases both above and below. The increase of σ_u far above and below the turbine are likely due to processes unrelated to the turbines, highlighting the challenges of stable boundary later simulation. More significant discrepancies are observed at $L2$, with the observation showing significant enhancements at all heights below 160 m not captured by the simulations. The intermittently large enhancements of σ_u at $L2$ at heights between 80 and 120 m increase in frequency and magnitude, with the peak increase occurring closer to the surface, with increasing λ. The observed increase of σ_u farther aloft is likely due to processes independent of the turbine, possibly waves or meandering motions occurring in the stable environment aloft.

Some explanation for the discrepancies between the $L2$ U and σ_u values obtained from the simulations is provided in Figs. 9 and 11, the latter showing a portion of the simulation

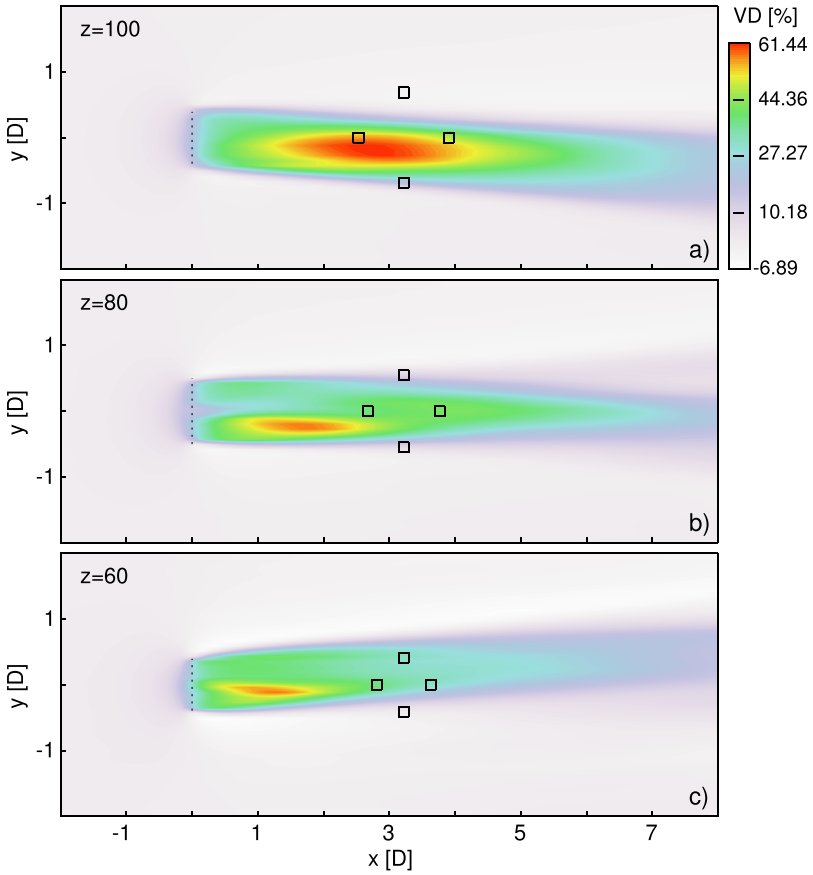

FIG. 11. Representative 10-min averaged horizontal cross sections of *VD* at three heights above the surface, from the stable simulation, as in Fig. 9.

averaged over 10 min. Figure 11 indicates that the lowest wake velocities are generally not sampled by the spanwise lidar beams. Additionally, at 80 m, the regions of lowest U tend not to mix into the wake center, which is dominated by faster flow channeled between the blades and the hub. While a nacelle drag parameterization (Aitken *et al.*, 2014b) was utilized, there is uncertainty in the optimal magnitude of the prescribed drag coefficient.

Simulations with GAD forces enhanced by 10%, to account for uncertainties in aerodynamic and operational parameters, showed slightly enhanced reductions of U at $L2$, but little impact on λ or σ_u (not shown). This suggests that generic aspects of the GAD, and particulars of the simulation setup utilized herein, more strongly influence the results than incorrect GAD parameter values.

B. Unstable case

Figure 12 shows instantaneous horizontal cross sections of U from the unstable simulations, as in Fig. 9. Here, $V_g = 13.0$ m s^{-1} and $\lambda_g = 35^\circ$ were used. Similar to Fig. 9, Fig. 12 shows reduced wind speeds downstream of the GAD, and while background fluctuations are much larger in the convectively forced flow, wake features still appear to intersect the $L2$ sampling beams only intermittently, with the wake not widening appreciably in the aggregate before reaching $L2$.

Figure 13 shows flow from a portion of the convective simulation averaged over 10 min, as in Fig. 10. Figure 13 indicates some acceleration of wake spreading relative to the stable simulation, however the beams perpendicular to the line between the GAD and $L2$ again do not encounter significantly reduced flow speeds on average.

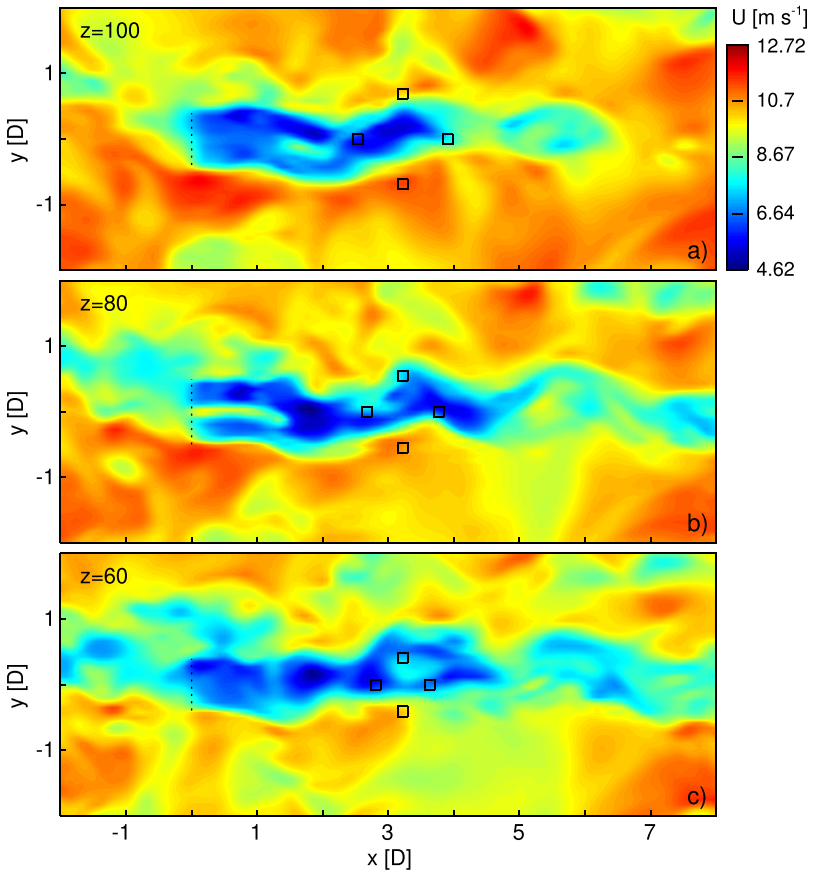

FIG. 12. Representative instantaneous horizontal cross sections of U at three heights above the surface, from the unstable simulations, as in Fig. 9.

Figure 14 shows 2-min average profiles of U (left), λ (middle), and σ_u (right) from 1 h of the unstable simulation, as in Fig. 10. While $\lambda_g = 35^\circ$ resulted in flow in near alignment with the observed mean value at L1, the temporal variability of simulated λ was only a few degrees (not shown). To produce a wider range of simulated inflow directions, two different values of $\lambda_g = 32.5^\circ$ and $\lambda_g = 37.5^\circ$ were used. Figure 14 shows 15 2-min average profiles taken from simulations using each value of λ_g.

Differences between the stable and unstable cases include a much wider range of all observed parameters at both $L1$ and $L2$, consistent with the strong mixing and variability characteristic of convective conditions. Although the simulations exhibit increased variability relative to the stable simulations, it is still significantly less than was observed, even using two values of λ_g, likely due to limitations of the idealized setup. Incorporating more realistic representations of environmental drivers of variability into the simulations (e.g., mesoscale features and surface characteristics) would likely increase the variability. As with the stable case, while the range of values is underrepresented, the magnitudes of the simulated U (left) and λ (middle) profiles at $L1$ are consistent with the observations. Simulated σ_u values (right) are again much smaller upstream, and again exhibit only modest increases at $L2$ relative to their upstream values.

V. DISCUSSION AND CONCLUSIONS

Changes of wind speed, direction, and variance of the streamwise velocity component in the near-wake region of an operating wind turbine are simulated using a large-eddy simulation model with a generalized actuator disk wind turbine parameterization. Simulations of one stable and one convective case study from the Crop Wind Energy Experiment of 2011 were conducted

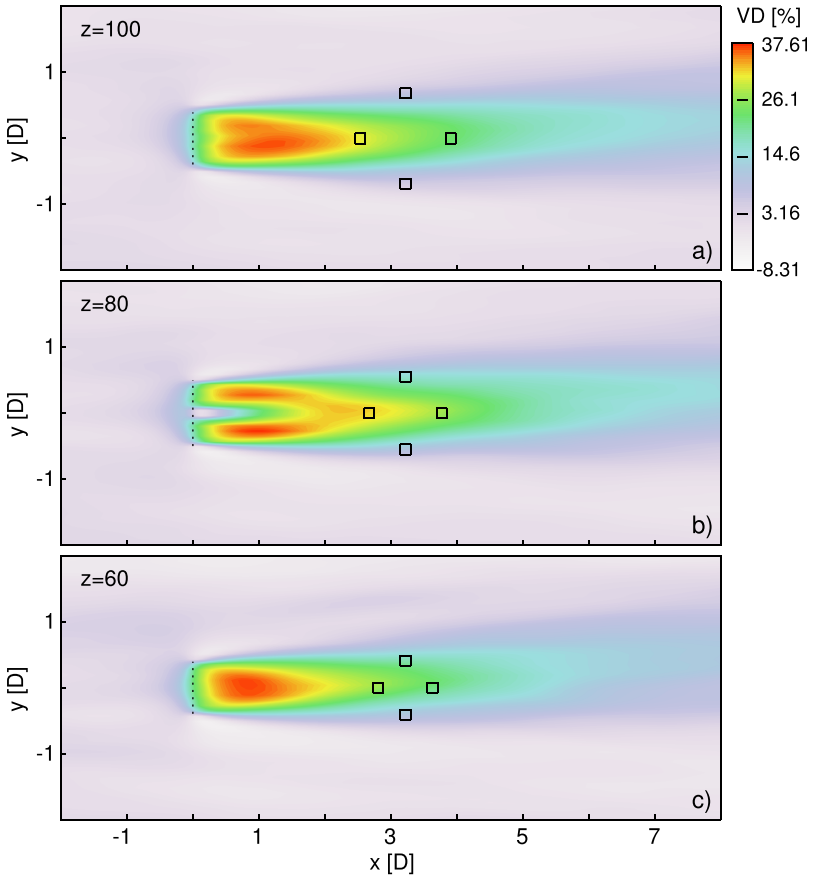

FIG. 13. Representative 10-min averaged horizontal cross sections of *VD* at three heights above the surface, from the unstable simulations, as in Fig. 11.

to evaluate the utility of velocity-azimuth display data from commercial Doppler profiling lidar systems to turbine wake characterization and model validation studies.

The simulations qualitatively capture many of the observed features of the two case studies, including similar profile shapes and ranges of values of U and λ at $L1$. Values of σ_u within the rotor swept area likewise agree reasonably well at $L1$ during the stable case study. Simulated σ_u values did not duplicate the observed increases near the surface or aloft at $L1$ during the stable case study, and were significantly smaller at all heights during the unstable case study.

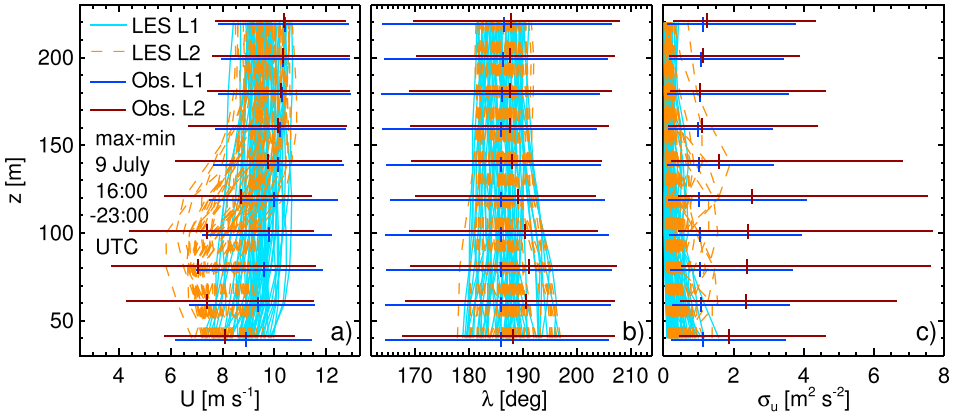

FIG. 14. 2-min average profiles of U (left), λ (middle), and σ_u (right) from 1 h of the unstable simulation, as in Fig. 11.

The simulations likewise reasonably captured the impacts of the turbine on *VD* values at *L*2 during both case studies, including larger and more persistent values during stable conditions. Inspection of horizontal plane averages (Figs. 9 and 11–13) reveals velocity deficits in the wake consistent with observed values of greater than 60% (see Figs. 1–4). However, sampling of simulated wake characteristics in a manner consistent with the VAD lidar sampling technique employed by the lidars utilized herein resulted in the appearance of somewhat smaller wind speed reductions. These results appear to contradict those of Mirocha *et al.* (2014) and Aitken *et al.* (2014b), who used a similar simulation framework in previous wake studies during both weakly convective and stable conditions, and showed generally good agreement between simulated and observed wake properties. Key differences between the studies are that while the former used scanning lidar observations at several locations within the wake, and applied a wake recognition algorithm to plan-position indicator (PPI) and range-height indicator (RHI) lidar scans (Aitken *et al.,* 2014a; 2014b), the present study relied upon profiles derived from VAD scans at one location downwind.

To investigate the sensitivity of the simulated wake parameters to aspects of the VAD lidar sampling strategy, we followed Lundquist *et al.* (2015), who recommend considering only the streamwise flow component in the near-wake region, obtained using only the streamwise lidar beams. Due to the simulated inflow being nearly aligned with the streamwise lidar beams during the case studies investigated herein, resulting in very small values of the spanwise velocity component, the results of two-beam versus four-beam retrievals were only trivially different at heights within the rotor swept area (results not shown). We also examined direct sampling of the simulations using no weighting along the beams, which returned slightly larger velocity reductions at L2, especially at 100 and 120 m, slightly improving agreement with the observations. Significantly larger σ_u values at L2 were also obtained using the non-weighted retrievals at heights of 100 and 120 m, improving agreement with the observations at those heights; however, the large increases observed at lower heights were not captured by the non-weighted sampling (results not shown).

While the weighting function influences sampled wake parameters, limitations of the actuator disk wind turbine parameterization must also be considered. An actuator disk model imparts significant velocity fluctuations at the spatial scale of the blade length (see Figs. 9 and 12), rather than at the chord scale, as either a real operating turbine, or a blade-resolving model would. As such, the large local velocity deficits associated with tip vortices that occur in real turbine wakes are not generated in the simulated flow field using an actuator disk. Therefore, such structures are not sampled at the lidar beam locations utilized to evaluate the simulated flows. The absence of such intense, small-scale structures in the flow field downstream of an actuator disk would be expected to underrepresent the variance, and could bias retrieved wind speeds toward higher values.

An additional factor impacting the ability of the simulations conducted herein to represent the observed variance is the use of relatively coarse grid spacings of 6 m, resulting in the GAD comprising at most 13 model grid points along horizontal and vertical lines intersecting the hub, with fewer grid points falling within the GAD perimeter elsewhere within the disk. As the WRF model has been shown to have an effective resolution of approximately 6–7 Δx (e.g., Skamarock (2004)), the LES at the spatial resolution specified herein cannot represent flow structures with dimensions much smaller than the GAD radius. The smaller σ_u values during the unstable case study might also reflect the relatively small computational domains employed, which only spanned approximately 1 km in the spanwise direction, which could have constrained the largest turbulence structures, those responsible for the largest deviations.

GAD models can be used with relatively coarse model resolutions (e.g., 8 grid cells within the rotor swept area, following, e.g., Wu and Porté Agel (2011)) to provide accurate simulations of aggregate wake characteristics. However, results herein reveal that aspects of the downstream flow field in the near wake region, especially those influencing σ_u, are not well captured using such an approach. Likely causes of the discrepancies between the simulations and observations include the absence of small-scale near wake physics and resulting flow structures, due to both the inherent nature of the GAD model, and the relatively coarse resolution, and, to a lesser but

still important extent, aspects of the VAD lidar-based sampling approach utilized herein. Future studies will investigate the roles of sampling strategy, model resolution and turbine parameterization type on the representation of near-wake physics, and the impacts thereof on small-scale wake structures and downstream wake retrievals, using the WRF simulation framework at higher spatial resolutions, and using an actuator line variant of the GAD.

ACKNOWLEDGMENTS

This work was performed under the auspices of the U.S. Department of Energy by Lawrence Livermore National Laboratory under Contract No. DE-AC52-07NA27344, and was supported by the U.S. DOE Office of Energy Efficiency and Renewable Energy, and the LLNL Graduate Scholars Program. NREL is a national laboratory of the U.S. Department of Energy, Office of Energy Efficiency and Renewable Energy, operated by the Alliance for Sustainable Energy, LLC. Data analysis was supported in part by the National Science Foundation under the State of Iowa EPSCoR Grant No. 1101284. The authors thank Sven Schmitz of Penn State University for the parameters of the 1.5 MW turbine used in the simulations. We also thank the team who collected the CWEX-11 dataset, including Matthew Aitken, Russell Doorenbos, Thomas Horst, Steven Oncley, Michael Rhodes, Eugene Takle, and Kristopher Spoth.

APPENDIX A: TURBULENT STRESSES AND SURFACE SIMILARITY

Monin-Obukhov similarity theory (Monin and Obukhov, 1954) is used to model exchanges of heat and momentum at the surface. When observed H_S values are prescribed, surface u_* values are determined from $\tau^s_{i3} = -C_D U(z_1) u_i(z_1)$, where $U(z_1)$ and $u_i(z_1)$ are the resolved horizontal wind speed and zonal and meridional velocity components, respectively, at their first computed heights above the surface, z_1, and $C_D = \kappa^2 [\ln\left(\frac{z_1+z_0}{z_0}\right) - \psi_M\left(\frac{z_1}{L}\right)]^{-2}$ with z_0 the roughness length. Following Arya (2001), $\psi_M\left(\frac{z}{L}\right) = \ln\left[\left(\frac{1+\chi^2}{2}\right)\left(\frac{1+\chi}{2}\right)^2\right] - 2\tan^{-1}(\chi) + \frac{\pi}{2}$, with $\chi = \left(1 - 15\frac{z}{L}\right)^{1/4}$. During stable conditions $\psi_M\left(\frac{z}{L}\right) = -5z/L$, with u_* computed analogously. When forced with a surface cooling rate ΔT_S, $H_S = -C_D U(z_1)[\theta_S - \theta(z_1)]$, where θ_S and $\theta(z_1)$ are the values of the potential temperature at the surface and the first grid point above, respectively.

The subgrid fluxes of momentum, M, above the surface, are given by the NBA (Kosović, 1997 and Mirocha *et al.*, 2010) model,

$$M_{ij} = -(C_S l)^2 \left\{ \begin{array}{l} 2\left(2\tilde{S}_{mn}\tilde{S}_{mn}\right)^{1/2}\tilde{S}_{ij} \\ \quad + C_1\left(\tilde{S}_{ik}\tilde{S}_{kj} - \frac{1}{3}\tilde{S}_{mn}\tilde{S}_{mn}\delta_{ij}\right) + C_2\left(\tilde{S}_{ik}\tilde{R}_{kj} - \tilde{R}_{ik}\tilde{S}_{kj}\right) \end{array} \right\}.$$

Here, $\tilde{S}_{ij} = \frac{1}{2}\left(\frac{\partial \tilde{u}_i}{\partial x_j} + \frac{\partial \tilde{u}_j}{\partial x_i}\right)$ and $\tilde{R}_{ij} = \frac{1}{2}\left(\frac{\partial \tilde{u}_i}{\partial x_j} - \frac{\partial \tilde{u}_j}{\partial x_i}\right)$ are the resolved strain-rate and rotation-rate tensors, respectively, with tildes indicating resolved components of the indicated flow parameter. The model constants are given by $C_S = \left(\frac{8(1+C_b)}{27\pi^2}\right)^{1/2}$, $C_1 = C_2 = \frac{960^{1/2}C_b}{7(1+C_b)S_k}$, $C_e = \left(\frac{8\pi}{27}\right)^{1/3} C_S^{4/3}$, and the skewness parameter, $S_k = 0.5$. Each of the constants are given as a function of a single parameter, the backscatter coefficient $C_b = 0.36$, and are formulated such that proper normal stresses are obtained for sheared homogeneous turbulence.

Subgrid fluxes of heat were prescribed using the Smagorinsky closure (Smagorinsky (1963) and Lilly (1967)), given by $\overline{u'_j \theta'_{v,j}} = -2K_q \frac{\partial \tilde{\theta}_v}{\partial x_j}$, where K_q is the eddy viscosity coefficient for scalar q, given by $K_q = P_r^{-1} K_M$, where $K_M = (C_S l)^2 max(0, |\tilde{S}_{ij}| - P_r^{-1} N^2)$ is the eddy viscosity coefficient for momentum, with $C_S = 0.18$ a constant, $l = (\Delta x \Delta y \Delta z)^{1/3}$ a length scale (isotropic), $P_r^{-1} = 3$ the inverse of the turbulent Prandtl number, and $N^2 = (g/\theta_{v0})/(\partial \tilde{\theta}_v/\partial z)$ the Brunt-Väisälä frequency.

APPENDIX B: SIMULATED LIDAR VELOCITY RETRIEVALS

The lidar was deployed such that the four beams were oriented in the four cardinal directions, at an angle of $\theta = 28^\circ$ with respect to the vertical direction. Along each beam, at each model height, the component of the flow vector projected onto each beam $V_{r,\propto}(z)$, $\propto \in$[N, S, E, W], identifying the north, south, east and west facing beams, respectively, was computed using bilinearly interpolated values of the streamwise (u) or spanwise (v) velocity component on surrounding model grid points. $V_\propto(z)$, the range-weighed value of the velocity component at each range gate z_R was computed as

$$V_\propto(z) = \int_{z_a}^{z_b} W(z) V_{r,\propto}(z) dz, \tag{B1}$$

where

$$W(z) = \frac{1}{c\tau_m}\left[erf\left(\frac{4\sqrt{\ln(2)}}{c\tau}(z - z_R) + \frac{\sqrt{\ln(2)}\tau_m}{\tau}\right) - erf\left(\frac{4\sqrt{\ln(2)}}{c\tau}(z - z_R) + \frac{\sqrt{\ln(2)}\tau_m}{\tau}\right)\right] \tag{B2}$$

describes the lidar weighting function at each model grid cell height z (Lundquist *et al.*, 2015). Here, z_a and z_b in Eq. (B1) describe heights at sufficient distances from each z_R beyond which the weighting function values becomes negligible, with $(z - z_R)$ in Eq. (B2) computed along the lidar beam. In Eq. (B2), c is the speed of light, τ_m is the range gate (265 ns), and τ is the Full Width Half Maximum (FWHM) (165 ns) pulse duration (Lundquist *et al.*, 2015).

With the assumption of horizontal homogeneity, the lidar-derived horizontal velocity components are computed as

$$u_L = \frac{V_E - V_W}{2\sin\theta} \quad \text{and} \quad v_L = \frac{V_N - V_S}{2\sin\theta}.$$

Aitken, M. L., Banta, R. M., Pichugina, Y., and Lundquist, J. K., "Quantifying wind turbine wake characteristics from scanning remote sensor data," J. Atmos. Oceanic Technol. **31**, 765–787 (2014a).

Aitken, M. L., Kosović, B., Mirocha, J. D., and Lundquist, J. K., "Large eddy simulation of wind turbine wake dynamics in the stable boundary layer using the weather research and forecasting model," J. Renewable Sustainable Energy **6**, 033137 (2014b).

Aitken, M. L. and Lundquist, J. K., "Utility-scale wind turbine wake characterization using nacelle-based long-range scanning lidar," J. Atmos. Oceanic Technol. **31**, 1529–1539 (2014).

Aitken, M. L., Rhodes, M. E., and Lundquist, J. K., "Performance of a wind-profiling lidar in the region of wind turbine rotor disks," J. Atmos. Oceanic Technol. **29**, 347–355 (2012).

Arya, S. P., *Introduction to Micrometeorology*, 2nd ed. (Academic Press, San Diego, 2001).

Barthelmie, R. J., Folkerts, L., Ormel, T., Sanderhoff, P., Eecen, P. J., Stobbe, O., and Nielsen, N. M., "Offshore wind turbine wakes measured by sodar," J. Atmos. Oceanic Technol. **20**, 466–477 (2003).

Basu, S., Holtslag, A. A. M., Van de Wiel, B. J. H., Moene, A. F., and Steeneveld, G.-J., "An inconvenient 'truth' about using sensible heat flux as a surface boundary condition in models under stably stratified regimes," Acta Geophys. **56**, 88–99 (2008).

Churchfield, M., Draxl, C., and Mirocha, J. D., "A one-way meso-microscale coupling strategy for realistic wind plant aerodynamics large-eddy simulation," J. Renewable Sustainable Energy (submitted).

Churchfield, M. J., Lee, S., Michalakes, J., and Moriarty, P. J., "A numerical study of the effects of atmospheric and wake turbulence on wind turbine dynamics," J. Turbul. **13**(14), N14 (2012).

Elliott, D. L. and Barnard, J. C., "Observations of wind turbine wakes and surface roughness effects on wind flow variability," Sol. Energy **45**, 265–283 (1990).

Hansen, K. S., Barthelmie, R. J., Jensen, L. E., and Sommer, A., "The impact of turbulence intensity and atmospheric stability on power deficits due to wind turbine wakes at Horns Rev wind farm," Wind Energy **15**, 183–196 (2012).

Hirth, B. M., Schroeder, J. L., Gunter, S., and Guynes, J., "Measuring a utility scale turbine wake using the TTUKa mobile research radars," J. Atmos. Oceanic Technol. **29**, 765–771 (2012).

Högström, U., Asimakopoulos, D. N., Kambezidis, H., Helmis, C. G., and Smedman, A., "A field study of the wake behind a 2 MW wind turbine," Atmos. Environ. **22**, 803–820 (1988).

Holton, J. R., *An Introduction to Dynamic Meteorology, Third Edition* (Academic Press, 1992).

Iungo, G., Wu, Y.-T., and Porté-Agel, F., "Field measurements of wind turbine wakes with lidars," J. Atmos. Oceanic Technol. **30**, 274–287 (2013).

Kosović, B., "Subgrid-scale modeling for the large-eddy simulation of high-Reynolds-number boundary layers," J. Fluid Mech. **336**, 151–182 (1997).

Lilly, D. K., "The representation of small-scale turbulence in numerical experiment," *Proceedings of the IBM Scientific Computing Symposium on Environmental Sciences* (IBM, New York, 1967), pp. 195–210.
Lundquist, J. K., Churchfield, M., Lee, S., and Clifton, A., "Quantifying error of lidar and sodar Doppler beam swinging measurements of wind turbine wakes using computational fluid dynamics," Atmos. Meas. Tech. **8**, 907–920 (2015).
Magnusson, M. and Smedman, A., "Influence of atmospheric stability on wind turbine wakes," Wind Eng. **18**(3), 139–152 (1994).
Mahrt, L. and Vickers, D., "Contrasting vertical structures of nocturnal boundary layers," Boundary-Layer Meteorol. **105**, 351–362 (2002).
Mehta, D., van Zuijlen, A. H., Koren, B., Holierhoek, J. G., and Bijl, H., "Large eddy simulation of wind farm aerodynamics: A review," J. Wind Eng. Ind. Aerodyn. **133**, 1–17 (2014).
Mirocha, J. D., Kosović, B., Aitken, M. L., and Lundquist, J. K., "Implementation of a generalized actuator disk wind turbine model into the weather research and forecasting model for large-eddy simulation applications," J. Renewable Sustainable Energy **6**, 013104 (2014).
Mirocha, J. D., Lundquist, J. K., and Kosović, B., "Implementation of nonlinear subfilter turbulence stress models for large-eddy simulations in the advanced research WRF model," Mon. Weather Rev. **138**, 4212–4228 (2010).
Monin, A. S. and Obukhov, A. M., "Basic laws of turbulent mixing in the surface layer of the atmosphere," Tr. -Akad. Nauk SSSR Geofiz. Inst. **24**, 163–187 (1954), English translation by John Miller, 1959.
Nygaard, N. G., "Lidar wake measurements in an onshore wind farm," in VindKraftNet: Remote Sensing Workshop, Roskilde, Denmark, 2011.
Rajewski, D. A., Takle, E. S., Lundquist, J. K., Oncley, S., Prueger, J. H., Horst, T. W., Rhodes, M. E., Pfeiffer, R., Hatfield, J. L., Spoth, K. K., and Doorenbos, R. K., "Crop wind energy experiment (CWEX): Observations of surface-layer, boundary layer, and mesoscale interactions with a wind farm," Bull. Am. Meteorol. Soc. **94**, 655–672 (2013).
Rajewski, D. A., Takle, E. S., Lundquist, J. K., Prueger, J. H., Pfeiffer, R. L., Hatfield, J. L., Spoth, K. K., and Doorenbos, R. K., "Changes in fluxes of heat, H_2O, and CO_2 caused by a large wind farm," Agric. For. Meteorol. **194**, 175–187 (2014).
Rhodes, M. E. and Lundquist, J. K., "The effect of wind turbine wakes on summertime midwest atmospheric wind profiles," Boundary-Layer Meteorol. **149**, 85–103 (2013).
Sanderse, B., van der Pijl, S. P., and Koren, B., "Review of computational fluid dynamics for wind turbine wake aerodynamics," Wind Energy **14**, 799–819 (2011).
Sathe, A., Mann, J., Gottschall, J., and Courtney, M., "Can wind lidars measure turbulence?," J. Atmos. Oceanic Technol. **28**(7), 853–868 (2011).
Schmitz, S., "XTURB-PSU: A wind turbine design and analysis tool," 2012, see http://www.aero.psu.edu/Faculty_Staff/schmitz/XTurb/XTurb.html.
Skamarock, W. C., "Evaluating mesoscale NWP models using kinetic energy spectra," Mon. Weather Rev. **132**, 3019–3032 (2004).
Skamarock, W. C. *et al.*, "A description of the advanced research WRF version 3," Report No. NCAR/TN-4751STR, National Center for Atmospheric Research, Boulder, CO, 2008.
Smagorinsky, J., "General circulation experiments with the primitive equations," Mon. Wea. Rev. **91**, 99 –152 (1963).
Smalikho, I. N., Banakh, V. A., Pichugina, Y. L., Brewer, W. A., Banta, R. M., Lundquist, J. K., and Kelley, N. D., "Lidar investigation of atmosphere effect on a wind turbine wake," J. Atmos. Oceanic Technol. **30**, 2554–2570 (2013).
Thomsen, K. and Sørensen, P., "Fatigue loads for wind turbines operating in wakes," J. Wind Eng. Ind. Aerodyn. **80**, 121–136 (1999).
Troldborg, N., Larsen, G. C., Madsen, H. A., Hansen, K. S., Sørensen, J. N., and Mikkelsen, R., "Numerical simulations of wake interaction between two wind turbines at various inflow conditions," Wind Energy **14**, 859–876 (2011).
Vanderwende, B., Lundquist, J. K., Rhodes, M. E., Takle, G. S., and Purdy, S. I., "Observing and simulating the summertime low-level jet in central Iowa," Mon. Weather Rev. **143**, 2319–2336 (2015).
Vermeer, L. J., Sørensen, J. N., and Crespo, A., "Wind turbine wake aerodynamics," Prog. Aerosp. Sci. **39**, 467–510 (2003).
Walton, R. A., Takle, E. S., and Gallus, W. A., Jr., "Characteristics of 50–200-m winds and temperatures derived from an Iowa Tall Tower Network," J. Appl. Meteorol. Climatol. **53**, 2387–2393 (2014).
Wu, Y. T. and Porté-Agel, F., "Large-eddy simulation of wind-turbine wakes: Evaluation of turbine parametrisations," Boundary-Layer Meteorol. **138**, 345–366 (2011).